



## In-vacancy engineered plate-like In(OH)<sub>3</sub> for effective photocatalytic reduction of CO<sub>2</sub> with H<sub>2</sub>O vapor



Bingbing Hu<sup>a</sup>, Maocong Hu<sup>c</sup>, Qiang Guo<sup>a</sup>, Kang Wang<sup>b</sup>, Xitao Wang<sup>a,\*</sup>

<sup>a</sup> Collaborative Innovation Center of Chemical Science and Engineering (Tianjin), Tianjin Key Laboratory of Applied Catalysis Science and Technology, College of Chemical Engineering and Technology, Tianjin University, Tianjin, 300072, China

<sup>b</sup> Chemical Engineering research center, College of Chemical Engineering and Technology, Tianjin University, Tianjin, 300072, China

<sup>c</sup> Shenzhen Joylong Contamination Control Co. Ltd., Joylong Institute of Industrial Technology, Shenzhen, 518000, China

### ARTICLE INFO

#### Keywords:

Photocatalytic reduction of CO<sub>2</sub>  
In(OH)<sub>3</sub>  
Indium vacancy  
Ethylenediamine

### ABSTRACT

In this work, a series of In(OH)<sub>3</sub> with abundant indium vacancies were synthesized by hydrothermal method using mixed solvent of ethylenediamine(En) and water for photocatalytic reduction of CO<sub>2</sub> with H<sub>2</sub>O vapor. The morphology, particle size, crystallinity, pore structure, and vacancy concentration of photocatalysts were successfully regulated by adjusting the ratio of En and water in mixed solvent, which were characterized by XRD, FT-IR, TG-DTA, SEM, HRTEM, UV-vis DRS, PL spectra, XPS, and EPR. Moreover, the effect of En/water ratio on the adsorption capacity to CO<sub>2</sub> and photo-electrical properties of In(OH)<sub>3</sub> were further investigated by in-situ FTIR, PL spectra, UV-vis DRS, CV, and EIS. In(OH)<sub>3</sub> prepared in mixed solution exhibited much higher photocatalytic activity for CO<sub>2</sub> reduction with H<sub>2</sub>O vapor compared to that prepared with water only solvent. The enhanced photocatalytic performance can be attributed to the special morphology, smaller particle size, larger BET surface area, and especially generated indium vacancies creating defect energy levels in the bandgap, which improved visible light absorption, carrier separation, and CO<sub>2</sub> chemisorption. This work paves the way to enable a non-visible-light response material with high visible-light photocatalytic activity by regulating vacancy concentration via a facile method.

### 1. Introduction

Photocatalytic CO<sub>2</sub> reduction coupled with the splitting of H<sub>2</sub>O to produce fuel such as CH<sub>4</sub>, CO and H<sub>2</sub>, etc. using solar energy has been widely accepted as one of the most attractive strategies to address environmental concerns and energy shortages [1–5]. However, the conversion efficiencies over the existing photocatalysts are usually low due to the fact that the activation and conversion of CO<sub>2</sub> is thermodynamically difficult while the C–O bond cleavage requires a high activation energy of about 220–330 kJ·mol<sup>-1</sup> [6–9]. Moreover, CO<sub>2</sub> showed weak interaction with most inorganic photocatalysts while it easily desorbed even at room temperature, leading to a low reaction rate and inferior photocatalytic efficiency. Therefore, developing high performance photocatalysts enabling electrons and holes generation with stronger redox ability as well as possessing better chemisorption performance to CO<sub>2</sub> molecule are very of importance in photocatalytic CO<sub>2</sub> reduction.

It is well known that an effective photocatalyst must have good light absorption, proper band structure, and low recombination rate of

photogenerated electron and hole, which strongly depend on the microstructure of material including composition, crystal structure, morphology, and defect, etc [10–12]. Although many semiconductors with narrow band gaps possess superior light absorption performance, they usually exhibit low quantum efficiency in photocatalytic CO<sub>2</sub> reduction owing to high recombination of photogenerated carriers, weak chemisorption ability, and inferior reduction or oxidation capacity of photogenerated electron or hole. In contrast, some semiconductors with wide band gaps can produce photogenerated electron and hole with sufficiently strong redox ability, but their weak light absorption severely constrains the photocatalytic performance. Defect engineering on semiconductors with wide band gap is an effective method for improving light absorption and separation efficiency of photogenerated carriers, resulting into superior photocatalytic activity [13–15]. For example, the existence of defects sites would narrow band gap by introducing new energy levels and enhance the light absorption, as well as prevent the recombination of photogenerated charge carriers. Notably, vacancies can improve the chemisorption and activation of CO<sub>2</sub> and H<sub>2</sub>O. CO<sub>2</sub>, as a Lewis acid, would be chemisorbed on cation

\* Corresponding author.

E-mail address: [wangxt@tju.edu.cn](mailto:wangxt@tju.edu.cn) (X. Wang).

vacancies, which act as active Lewis basic sites, by Lewis acid-base interactions to form  $\text{CO}_3^{2-}$  species. Simultaneously,  $\text{H}_2\text{O}$  is a Lewis base donating a pair of nonbonding electrons while the oxygen vacancies ( $V_{\text{O}}$ ) serve as active Lewis acidic sites, leading to the formation of the other Lewis acid-base interactions [16]. As a result, the photocatalytic activity of semiconductor was enhanced. Many previous works have reported the positive effects of defect vacancies for the photocatalytic reaction over various photocatalysts including  $\text{TiO}_2$  [17],  $\text{ZnO}$  [18],  $\text{Fe}_2\text{O}_3$  [19],  $\text{BiOCl}$  [20],  $\text{ZnS}$  [21–23],  $\text{g-C}_3\text{N}_4$  [24], and  $\text{La(OH)}_3$  [25] etc. Therefore, vacancy engineering is a potential approach for enhancing the light absorption behavior and photocatalytic activity of photocatalyst even with wide band gap.

Indium compounds ( $\text{In(OH)}_3$ ,  $\text{InOOH}$ , and  $\text{In}_2\text{O}_3$ ) are an important class of semiconductor compounds and are widely used in many fields [26,27]. At present, there are many studies on the photocatalysis of  $\text{In}_2\text{O}_3$ , such as indium oxide with different morphologies [28] (nanosphere, nanorod, nanocore shell structure, etc.), composite of  $\text{In}_2\text{O}_3$  and other semiconductors [29–31] ( $\text{TiO}_2/\text{In}_2\text{O}_3$ ,  $\text{WO}_3/\text{In}_2\text{O}_3$ ,  $\text{p-CuO/n-Cu}_{1-x}\text{In}_x\text{O}_3$ , etc.) and metal and non-metal elements doped  $\text{In}_2\text{O}_3$  [32–35] (Pt-decorated  $\text{In}_2\text{O}_3$ , palladium/  $\text{In}_2\text{O}_3$ , N, Co co-doped  $\text{In}_2\text{O}_3$ , etc.). However,  $\text{In(OH)}_3$ , as a wide bandgap semiconductor (5.2 eV), is usually used as intermediate in hydrothermal synthesis of indium oxide materials and often overlooked in past studies [36]. On the other hand, many studies show that metal hydroxides are relatively simple in fabrication process, and do not require post-heat treatment. Therefore, it would effectively maintain the original structure of metal hydroxides and the functional groups such as rich hydroxyl groups on surface [37]. These hydroxyl groups in  $\text{In(OH)}_3$  benefit the activation of  $\text{H}_2\text{O}$  molecule, which may promote the photocatalytic  $\text{CO}_2$  reduction with  $\text{H}_2\text{O}$ . However, to the best of our knowledge, direct use of  $\text{In(OH)}_3$  as a photocatalyst as well as the investigation of creating vacancies in  $\text{In(OH)}_3$  and their influence on the band structure and photocatalytic activity have rarely been reported.

In present work, a series of indium hydroxide were synthesized by the hydrothermal method using mixed solution of ethylenediamine (En) and water as solvent. The morphologies and defect concentrations were regulated by adjusting En/water ratio in solvent. The effects of morphologies and defect concentrations on the light absorption, chemisorption of  $\text{CO}_2$ , photo-electrical property were systematically investigated by XRD, FT-IR, TG-DTA, SEM, HRTEM, EPR, XPS, in-situ FTIR, PL spectra, UV-vis DRS, CV and EIS. The photocatalytic performance of  $\text{In(OH)}_3$  under visible light was evaluated by photocatalytic  $\text{CO}_2$  reduction with  $\text{H}_2\text{O}$ .

## 2. Experimental

### 2.1. Photocatalyst preparation

All of the chemical reagents were of analysis grade and used without further purification. A series of indium hydroxides were synthesized by hydrothermal method. In a typical process, 0.88 g of  $\text{InCl}_3 \cdot 4\text{H}_2\text{O}$  (Kermel, AR) was first dissolved in deionized water with stirring for 10 min at room temperature, and then ethylenediamine (En, Aladdin, > 99%) was added to the solution under stirring, followed by ultrasonication for 20 min. The resulting solution was transferred into a 100 mL Teflon-lined stainless-steel autoclave and heated at 200 °C for 12 h. Subsequently, the autoclave was cooled to room temperature naturally. The obtained precipitate was washed with ethanol and deionized water for three times, respectively and dried at 50 °C for 12 h. The obtained  $\text{In(OH)}_3$  was white solid powder.

For all samples, the total volume of hydrothermal solvent was kept constant (75 mL) and the volume ratio of En/water was adjusted to 0:1, 1:1, 2:1, 3:1, 4:1 and 5:1, respectively. The obtained  $\text{In(OH)}_3$  samples were designated as 0/1- $\text{In(OH)}_3$ , 1/1- $\text{In(OH)}_3$ , 2/1- $\text{In(OH)}_3$ , 3/1- $\text{In(OH)}_3$ , 4/1- $\text{In(OH)}_3$  and 5/1- $\text{In(OH)}_3$ , respectively.

### 2.2. Characterization

The crystal structures and phase compositions of the samples were characterized by X-ray diffractometer (XRD), which was recorded on a Bruker AXS D8 powder diffractometer equipped with graphite monochromatized Cu K $\alpha$  radiation flux ( $\lambda = 0.15418 \text{ nm}$ , 40 kV, 200 mA) at a scanning rate of 8° min<sup>-1</sup> in the 20 range of 15–80°.

The morphology and size distribution were determined by means of scanning electron microscopy (SEM) (Hitachi S-4800, Japan, 5 kV). Transmission electron microscopy (TEM) and higher-magnification transmission electron microscopy (HRTEM) images were obtained using a JEOL JEM-2100 F field emission electron microscope operating at an accelerating voltage of 200 kV.

TG and DTA was carried out on a Perkin-Elmer Diamond TG instrument using platinum-platinum/rhodium thermocouple at a heating rate of 10 °C min<sup>-1</sup> in air. The sample amount was 10 mg and the air flow rate was 50 mL/min. Temperature measurement range from room temperature to 800 °C.

The Fourier transform infrared (FT-IR) spectra were recorded with Thermo Nicolet Nexus using the KBr disk method. In situ diffuse reflectance infrared spectroscopy experiments for  $\text{CO}_2$  chemisorption were performed by the specific operation steps as follows. A certain amount of catalysts was loaded to the in-situ infrared diffuse reflection sample cell to smooth the sample to enhance the diffuse reflection effect. The sample cell was first purged with helium (30 mL/min) at 200 °C for 1 h. Subsequently, the feed stream of  $\text{CO}_2$  (30 mL/min) was introduced for dynamic adsorption. The spectrum was acquired every 5 min until the infrared spectrum obtained did not change.

The surface areas and pore sizes were determined using a Quantachrome Autosorb, carried out at 77.3 K using  $\text{N}_2$  as an adsorbate. The samples were degassed at 473 K for 6 h before measurements. The Brunauer Emmett Teller (BET) equation was used to calculate the surface area. The Barrett Joyner Halenda (BJH) method was used to determine the pore-size distribution.

UV-vis spectra were measured on a PerkinElmer Lambda750 instrument at wavelengths of 200–800 nm by using  $\text{BaSO}_4$  as a reference.

Photoluminescence (PL) spectra were taken on a Fluorolog<sub>3</sub> photoluminescence spectrometer (Horiba Jobin Yvon, Japan) using a Xe lamp with an excitation wavelength of 325 nm at room temperature.

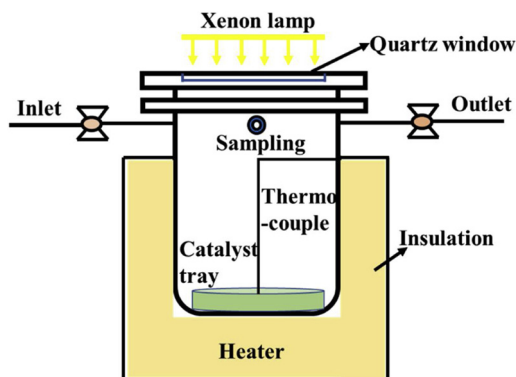
Photoelectrochemical measurements were performed in an electrochemistry workstation (CHI 660, CH Instrument, Austin, TX) with a three-electrode system using a three-compartment glass cell. Platinum electrode and Ag/AgCl electrode were used as the counter electrode and the reference electrode, respectively. A sample coated on ITO glass served as the working electrode. The experiments were operated at room temperature with  $\text{Na}_2\text{SO}_4$  solution (0.1 mol L<sup>-1</sup>) as electrolyte. A 300 W Xe lamp was used as the light source.

Electron paramagnetic resonance (EPR) spectra were recorded on a JEOL FA-200 EPR spectrometer at room temperature.

X-ray photoelectron spectroscopy (XPS) measurements were performed using ESCALAB 250Xi spectrometer. All binding energies were calibrated to the C 1 s peak at 284.8 eV.

### 2.3. Photocatalytic reduction of $\text{CO}_2$

Photocatalytic reduction of  $\text{CO}_2$  was carried out under the illumination of a xenon lamp with a 420 nm cutoff in a homemade airtight vessel made of stainless steel with quartz windows at the top (as shown in Scheme 1). In a typical experimental process, firstly, 50 mg of the catalyst was uniformly dispersed in the tray of the reactor. Prior to the irradiation, the reactor was flushed with  $\text{CO}_2$  (30 mL/min) for 2 h at 200 °C to remove air in the reactor and the organic species adsorbed on the surface of catalyst. The temperature of the reactor was monitored using a thermocouple. Finally, the valves at the gas inlet and outlet were closed and 0.3 mL of deionized water was injected into the reactor. After 4 h of irradiation at 200 °C, the products were analyzed by



**Scheme 1.** Schematic diagram of the reaction system for photocatalytic reduction of  $\text{CO}_2$  with  $\text{H}_2\text{O}$  vapour.

on-line gas chromatography using a thermal conductivity detector (Agilent 4890, nitrogen as a carrier gas).

### 3. Results and discussion

#### 3.1. Morphologies and structures of $\text{In}(\text{OH})_3$ semiconductors

Fig. 1A shows the XRD patterns of  $\text{In}(\text{OH})_3$  prepared by hydrothermal solvent with different En/water ratios. All samples displayed ten diffraction peaks at  $2\theta = 22.3^\circ, 31.7^\circ, 35.5^\circ, 39.1^\circ, 45.4^\circ, 51.2^\circ, 56.5^\circ, 66.2^\circ, 70.8^\circ$  and  $75.3^\circ$ , which can be ascribed to (200), (220), (013), (222), (400), (420), (440), (442), and (620) crystal faces of cubic  $\text{In}(\text{OH})_3$  (JCPDS 85–1338), respectively. No peaks from any other phases or impurities were detected, indicating that the prepared samples are pure body-centered cubic indium hydroxide. Obviously,  $\text{In}(\text{OH})_3$  prepared in water only solvent exhibited far stronger diffraction peaks when compared to other samples, showing higher crystallinity or

larger particle size. With the increase of En amount in solvent from 0/1 to 5/1, the intensity of the diffraction peaks gradually decreased, suggesting the low crystallinity and small particle size.

To further determine the composition and structure of  $\text{In}(\text{OH})_3$  samples synthesized in different solvents, TG-DTA analysis and FT-IR were performed. Fig. 1-B is thermal weight loss curves in static air atmosphere. 0/1- $\text{In}(\text{OH})_3$  has only one step with the weight loss of about 16%. It results from the loss of water during the conversion of  $\text{In}(\text{OH})_3$  to  $\text{In}_2\text{O}_3$ , based on the chemical equation  $2\text{In}(\text{OH})_3 \rightarrow \text{In}_2\text{O}_3 + 3\text{H}_2\text{O}$ . For  $\text{In}(\text{OH})_3$  prepared in mixed solution of En and water as solvent, there are two stages corresponding to the desorption/decomposition of different species. The first one ( $30\text{--}100^\circ\text{C}$ ) is mainly from the physical adsorbed En. The weight loss is 1.96%, 3.07%, 5.43%, 8.13%, respectively, for 1/1- $\text{In}(\text{OH})_3$ , 3/1- $\text{In}(\text{OH})_3$ , 4/1- $\text{In}(\text{OH})_3$ , and 5/1- $\text{In}(\text{OH})_3$ , indicating that the amount of residual En in the samples gradually increased with the increase of En/water ratios. The second stage ( $280\text{--}300^\circ\text{C}$ ) with loss of 15.78%, 14.93%, 14.86%, 14.68%, respectively, corresponds to the loss of water attributing to the decomposition of  $\text{In}(\text{OH})_3$  to  $\text{In}_2\text{O}_3$ . The DTA curves (Fig. 1-C) have two endothermic peaks. The first peak near  $80^\circ\text{C}$  can be attributed to the release of En while the second one at around  $300^\circ\text{C}$  derived from the thermal decomposition of  $\text{In}(\text{OH})_3$  to  $\text{In}_2\text{O}_3$ . It was also found that with the increase of En content, the peak near  $300^\circ\text{C}$  gradually weakened and broadened, indicating that the crystallinity of the sample gradually deteriorated. This result was consistent with the XRD patterns.

FT-IR spectrum in Fig. 1-D displays the characteristic absorption peaks of natural  $\text{In}(\text{OH})_3$  at  $3425\text{ cm}^{-1}$  (O–H stretching vibrations),  $827\text{ cm}^{-1}$  (O–H bending vibration),  $1161\text{ cm}^{-1}$ ,  $1107\text{ cm}^{-1}$  and  $505\text{ cm}^{-1}$  (In–OH absorption bands) [38], indicating that the synthetic sample is  $\text{In}(\text{OH})_3$ . The peak at  $2500\text{--}2000\text{ cm}^{-1}$  is from  $\text{CO}_2$  in air. Other peaks at  $1625$ ,  $1520$ ,  $1320$ ,  $1100$ ,  $635$ , and  $442\text{ cm}^{-1}$  correspond to absorption vibration of  $\text{NH}_2$ ,  $\text{CH}_2$ ,  $\text{C–N}$ , and  $\text{C–N–N–C}$  bonds, which result from the residual En [39,40].

The morphologies of  $\text{In}(\text{OH})_3$  prepared by varying the ratio of En/

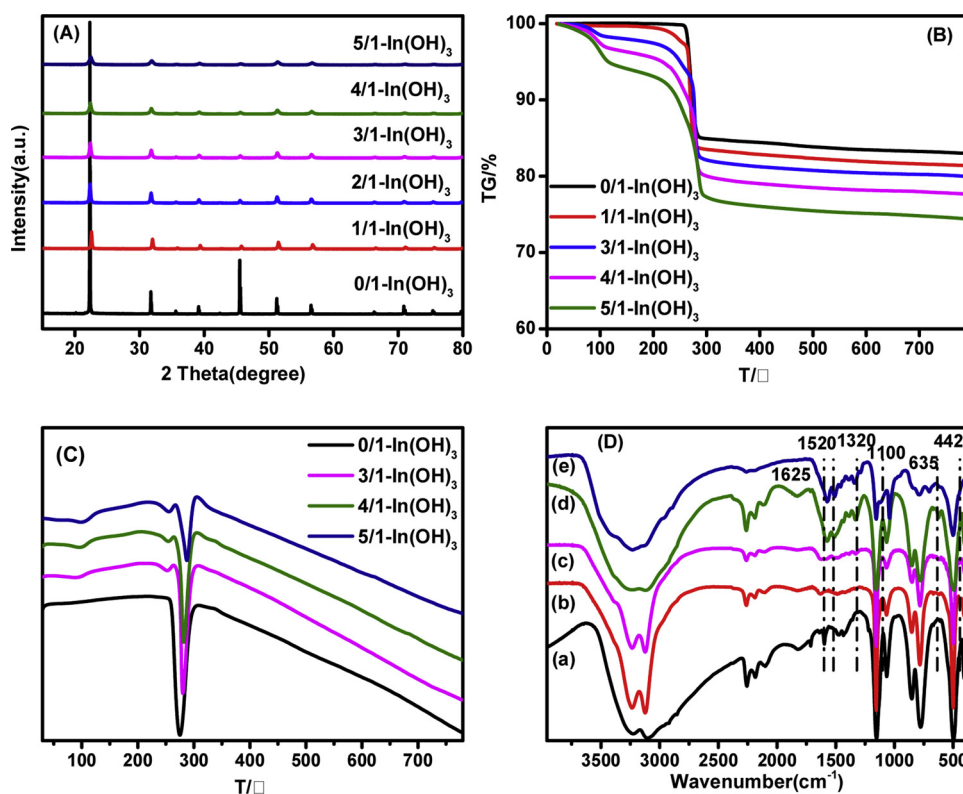


**Fig. 1.** (A) XRD patterns; (B) Thermal weight loss curves; (C) the DTA; and (D) the FT-IR of  $\text{In}(\text{OH})_3$  series((a) 0/1- $\text{In}(\text{OH})_3$ , (b)1/1- $\text{In}(\text{OH})_3$ , (c)3/1- $\text{In}(\text{OH})_3$ , (d)4/1- $\text{In}(\text{OH})_3$ , (e)5/1- $\text{In}(\text{OH})_3$ ).

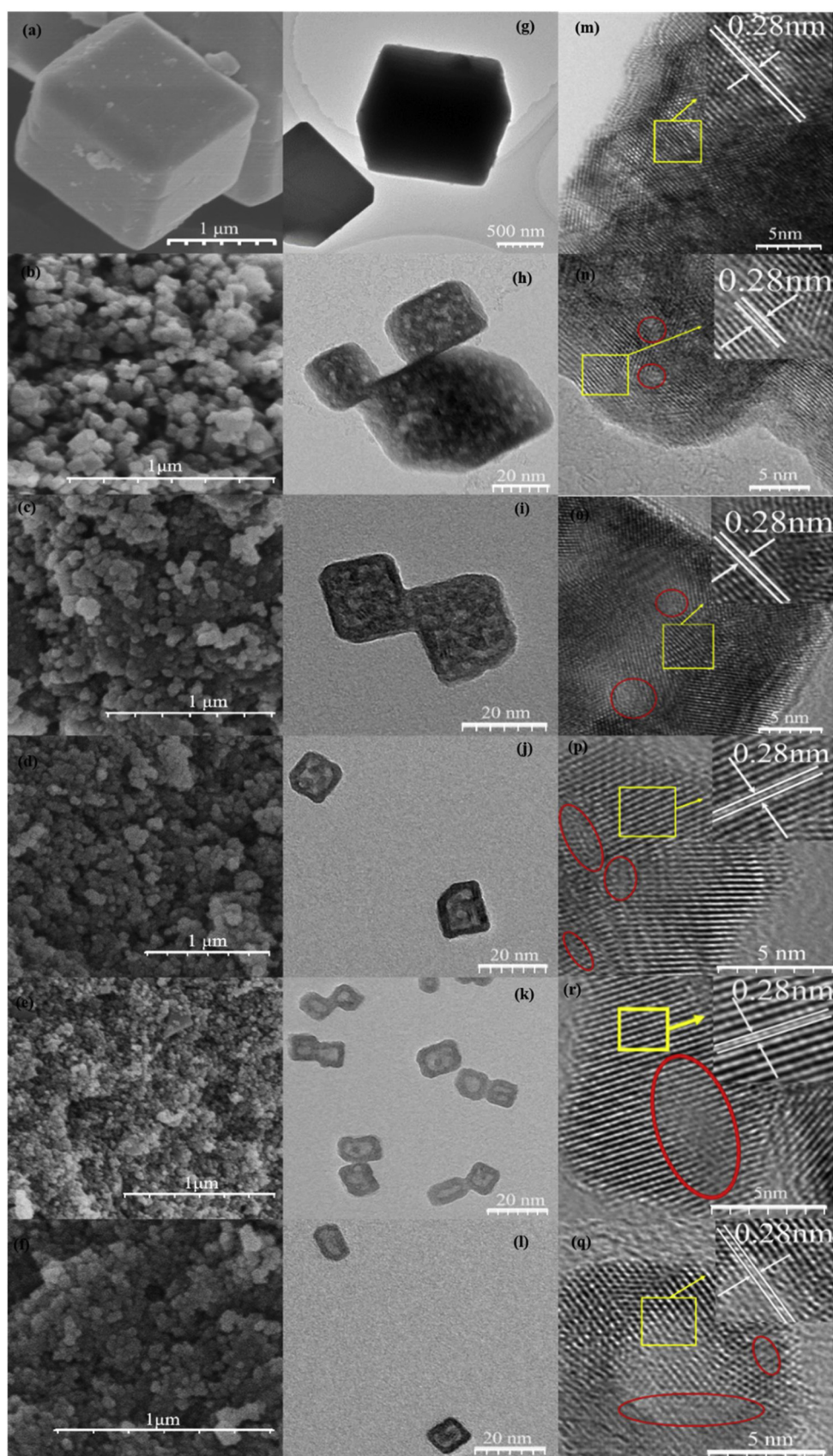
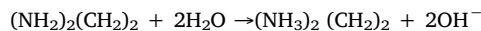


**Fig. 2.** SEM images of (a) 0/1- In(OH)<sub>3</sub>, (b) 1/1 In(OH)<sub>3</sub>, (c) 2/1- In(OH)<sub>3</sub>, (d) 3/1- In(OH)<sub>3</sub>, (e) 4/1- In(OH)<sub>3</sub>, (f) 5/1- In(OH)<sub>3</sub>; TEM images of (g) 0/1-In(OH)<sub>3</sub>, (h) 1/1 In(OH)<sub>3</sub>, (i) 2/1- In(OH)<sub>3</sub>, (j) 3/1- In(OH)<sub>3</sub>, (k) 4/1- In(OH)<sub>3</sub>, (l) 5/1- In(OH)<sub>3</sub>; and HR-TEM images of (m) 0/1-In(OH)<sub>3</sub>, (n) 1/1 In(OH)<sub>3</sub>, (o) 2/1- In(OH)<sub>3</sub>, (p) 3/1- In(OH)<sub>3</sub>, (q) 4/1- In(OH)<sub>3</sub>, (r) 5/1- In(OH)<sub>3</sub>.

water were characterized by FE-SEM, TEM, and HRTEM, as shown in Fig. 2. The sample prepared in water only solvent (0/1-In(OH)<sub>3</sub>) displayed regular cubic structure with smooth surface and edge length of about 1.0–1.5 μm (Fig. 2-a). The addition of En in solvent has significant influence on both particle sizes and morphologies. With the increase of En/water ratios from 0/1 to 5/1, particle sizes gradually decreased from 1.0 to 1.5 μm to about 40–50 nm, 25 nm, 20 nm, 15 nm, and 10 nm, respectively. Furthermore, the morphologies were successively changed from cube to irregular tetrahedron, lamella, and plate-like structure with pock-marked surface. Moreover, spacing values of lattice fringes observed in HRTEM images are 0.28 nm, corresponding to (220) crystal plane of cubic In(OH)<sub>3</sub>, which is consistent with XRD observations. In addition, the indiscernible lattice fringes observed in red circle regions of Fig. 2 n, o, p, q and r imply the existence of abundance of vacancies on the surface of In(OH)<sub>3</sub> nanoparticles, which will be further investigated by UV-vis DRS and PL techniques.

Studies showed that obtaining a uniform size distribution depends on competing nucleation and growth. Instantaneous nucleation leads to homogeneous particle growth while progressive nucleation leads to heterogeneous particle growth [41]. Under water only solvent condition, hydrolysis rate of In<sup>3+</sup> is very slow due to low pH value and OH<sup>-</sup> concentration, which results into progressive nucleation. As a result, the grain growth rate is much higher than the formation rate of In(OH)<sub>3</sub> crystal nucleus, leading to the production of larger particles. Moreover, the probability of crystal growth in all directions is equal, which leads the harvest of cubic morphology In(OH)<sub>3</sub> [42]. In a mixed system of water and En, the presence of En would increase environmental pH value and OH<sup>-</sup> concentration following chemical equations:



Thus, the hydrolysis rate of In<sup>3+</sup> became faster while a large number of In(OH)<sub>3</sub> crystal nucleus were formed, which made instantaneous nucleation be dominant. As a result, a low growth rate of In(OH)<sub>3</sub> grain was achieved. Consequently, smaller particles were formed. Moreover, En molecule containing coordinating group would be chemisorbed preferentially on the surface (one crystal face) of the formed In(OH)<sub>3</sub> nanoparticles. It would decrease crystal growth rate of the attached face, leading to formation of different morphologies. In some cases, the attached En would occupy sites belonging to In<sup>3+</sup> in crystal lattice, which led to the generation of vacancies as demonstrated in Fig. 2 (also confirmed in the next EPR and XPS measurement).

To further confirm above mechanism, physical property investigation on the pore structure and size distribution was conducted. Fig. 3 shows N<sub>2</sub> adsorption-desorption isotherm and BJH pore size

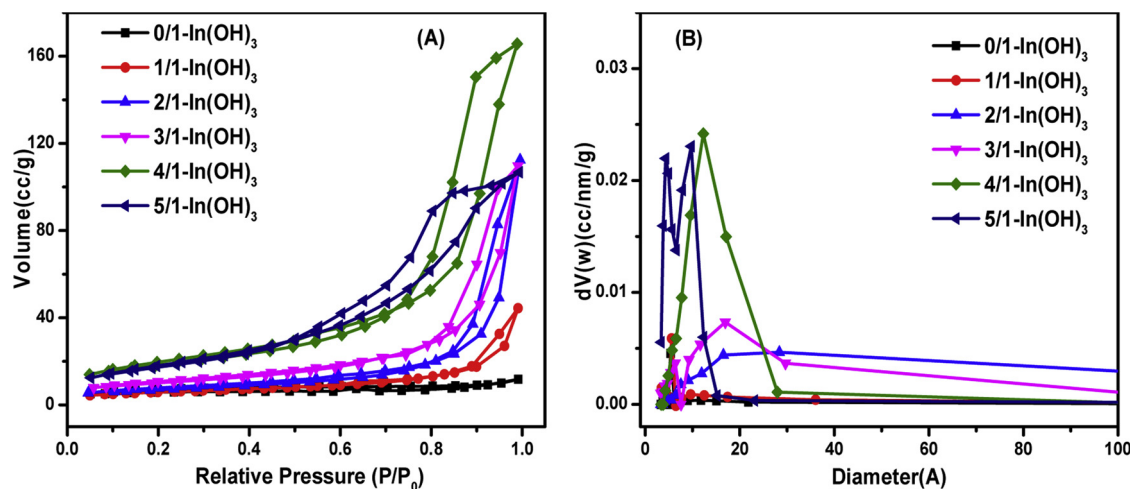


Fig. 3. (A) N<sub>2</sub> adsorption – desorption isotherms and (B) the pore size distributions of the In(OH)<sub>3</sub> series.

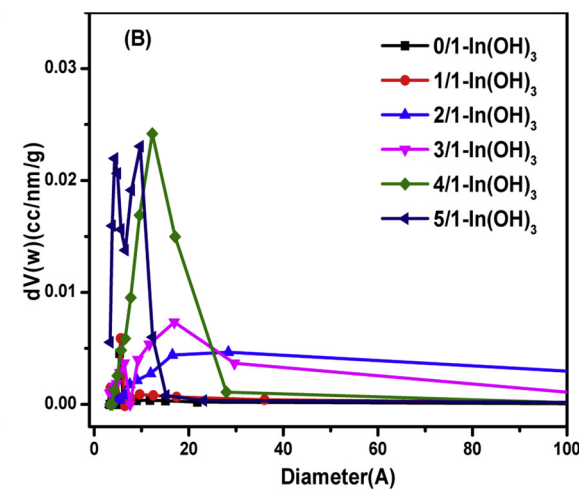
**Table 1**  
The results of N<sub>2</sub> adsorption and desorption experiment.

Catalysts	Specific surface area / (m <sup>2</sup> /g)	Total pore volume /(cm <sup>3</sup> /g)	Average aperture /nm
0/1-In(OH) <sub>3</sub>	24.0	0.0182	0.30
1/1-In(OH) <sub>3</sub>	26.7	0.0697	1.33
2/1-In(OH) <sub>3</sub>	27.9	0.1739	2.50
3/1-In(OH) <sub>3</sub>	38.6	0.1696	1.76
4/1-In(OH) <sub>3</sub>	71.2	0.2563	1.44
5/1-In(OH) <sub>3</sub>	67.5	0.1651	0.98

distribution curves. For 0/1-In(OH)<sub>3</sub> sample, neither hysteresis loop in adsorption-desorption isotherm nor obvious peak in pore distribution curve was observed, suggesting its no n-porous micro-structure. In contrast, samples prepared in mixed solution of En and water exhibited typical type IV adsorption-desorption isothermal curves (IUPAC classification) [43–44] with a distinct condensation step and a hysteresis loop, indicating the characteristic mesoporous structure. Moreover, with the increase of En addition amount, both the area of hysteresis loop and N<sub>2</sub> adsorption amount first increased and then decreased, showing that number of mesopores and surface areas increased first and then decreased. The pore distribution in Fig. 3-B has the same trend. BET specific surface areas, average diameters and pore volumes of In(OH)<sub>3</sub> samples were listed in Table 1. BET surface area of 0/1-In(OH)<sub>3</sub> sample is 24.0 m<sup>2</sup>/g, which are much lower than those of In(OH)<sub>3</sub> samples prepared in mixed solution of En and water. BET surface area of In(OH)<sub>3</sub> sample also shows volcano curves with the increase of En content. Pore volumes and average pore sizes of In(OH)<sub>3</sub> follow the same trend. All the physical properties demonstrated in this section indicate the positive effect of En introduction on pore formation of In(OH)<sub>3</sub>, while the excessive En (the case in 5/1-In(OH)<sub>3</sub>) may result into pore block and surface area decrease.

### 3.2. Optical and electronic properties of in(OH)<sub>3</sub> semiconductors

Room temperature PL spectroscopy was used to study the separation, migration, recombination processes of photogenerated electron hole pairs at room temperature as shown in Fig. 4-A. 0/1-In(OH)<sub>3</sub> showed limited luminescence under ultraviolet excitation, just as reported in previous paper that crystalline In(OH)<sub>3</sub> had no PL emission [45]. All In(OH)<sub>3</sub> prepared in mixed solution exhibited strong and broad PL peaks at the range of 375 nm to 550 nm. Since the band gap of In(OH)<sub>3</sub> is around 5.15 eV (corresponds to the photo-absorption of 240 nm), the emission at the range of 375 nm to 550 nm could be



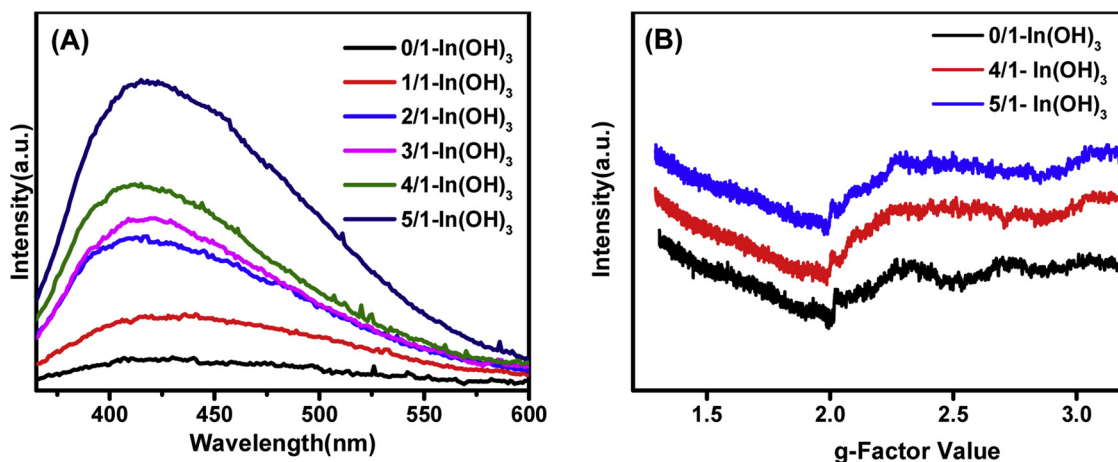


Fig. 4. (A) Room-temperature PL spectra; (B) EPR spectra.

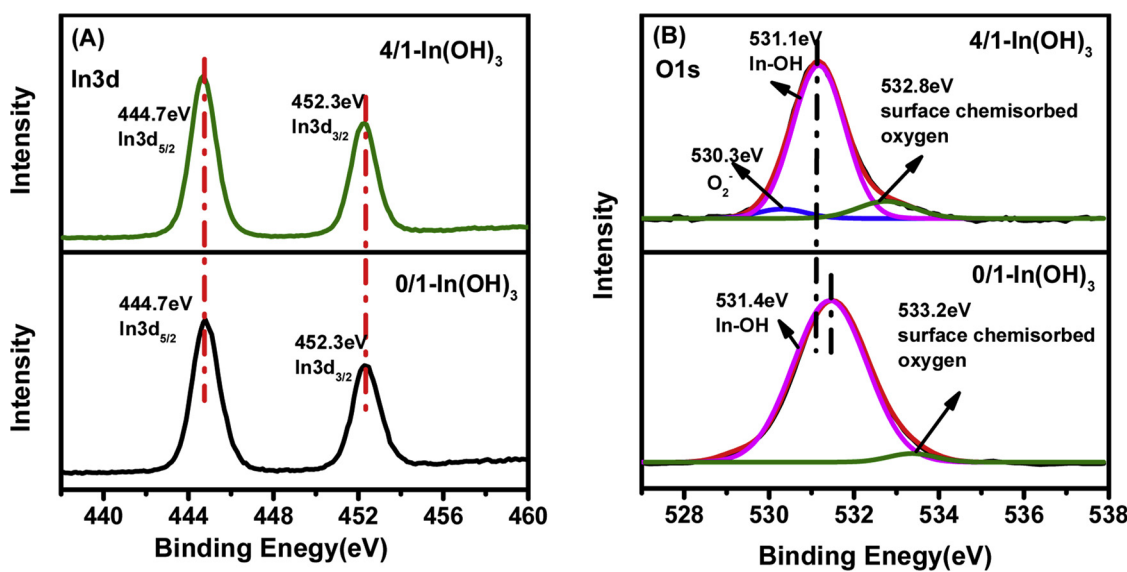
ascribed to In vacancy defect-states emission instead of the transition from conduction band to valence band within In(OH)<sub>3</sub>. Moreover, with the increase of En/water ratio in solvent, the emission intensity became stronger gradually, indicating the increase of defect concentration on the surface. The result is consistent with that observed by HRTEM. To further determine the type of defect, an Electron Paramagnetic Resonance (EPR) was performed as shown in Fig. 4-B. There are two possible vacancy types on the In(OH)<sub>3</sub> samples prepared with mixed solution: indium and oxygen vacancy. Compared to 0/1-In(OH)<sub>3</sub> sample, 4/1-In(OH)<sub>3</sub> and 5/1-In(OH)<sub>3</sub> samples show almost the same EPR signal intensity at g value of around 2, which is reported as g value of oxygen vacancy [46–48]. Therefore, it is reasonable to ascribe the light emission in PL to indium vacancy.

To further confirm the presence of indium vacancies, XPS spectra of 0/1-In(OH)<sub>3</sub> and 4/1-In(OH)<sub>3</sub> are performed, as shown in Fig. 5. Both 0/1-In(OH)<sub>3</sub> and 4/1-In(OH)<sub>3</sub> samples displayed almost the same binding energies for In 3d located at 444.7 eV and 452.3 eV, which are assigned to In 3d<sub>5/2</sub> and In 3d<sub>3/2</sub>, respectively [49]. However, the O1 s XPS spectra of 4/1-In(OH)<sub>3</sub> is obviously different with that of 0/1-In(OH)<sub>3</sub>. The O1 s XPS spectrum of 0/1-In(OH)<sub>3</sub> can be well fitted into two peaks at the binding energies of 533.2 and 531.4 eV, respectively, which can be attributed to the surface chemisorbed oxygen or H<sub>2</sub>O and In –OH. [50,51] These two peaks in 4/1-In(OH)<sub>3</sub> shifted towards to lower energy while a new XPS peak at 530.3 eV related to bridging

O<sub>2</sub><sup>2-</sup> is observed [52]. It indicates the existence of a number of unsaturated O atoms on the surface of 4/1-In(OH)<sub>3</sub> and further reveals the presence of In vacancy.

UV-visible diffuse reflectance spectrum was used to investigate the effects of vacancies on the optical properties. As shown in Fig. 6-A, 0/1-In(OH)<sub>3</sub> sample exhibited only absorption in ultraviolet region at the wavelength less than 240 nm, indicating that it possessed a band gap wider than 5.2 eV. The addition of En in solvent enhanced the light absorption of samples in the range of 260–350 nm, while a significant tailing absorption was detected in the range of 480–650 nm. The defect sites caused by the addition of En may contribute to the absorption of visible light. Furthermore, with increasing En/water ratio, the light absorption in visible region gradually improved, resulting from the increase of defect concentration. It further confirmed our hypothesis that defect concentration can be regulated by adjusting En/water ratio as illustrated in last section.

The corresponding band gap energies of In(OH)<sub>3</sub> samples prepared in different solvents are calculated by the transformed Kubelka-Munk function [53], as shown in Fig. 6-B. In(OH)<sub>3</sub> prepared in water only solvent has a band gap value of 5.21 eV, while In(OH)<sub>3</sub> samples prepared in mixed solution display two band gap energies of 5.28 and 2.89 eV, 5.24 and 2.84 eV, 5.15 and 2.76 eV, 4.92 and 2.71 eV for 2/1-In(OH)<sub>3</sub>, 3/1-In(OH)<sub>3</sub>, 4/1-In(OH)<sub>3</sub>, and 5/1-In(OH)<sub>3</sub>, respectively. The former one can be attributed to the main band gap from bulk In(OH)<sub>3</sub>

Fig. 5. XPS spectra of (A) In 3d, (B) O 1s for 0/1-In(OH)<sub>3</sub> and 4/1-In(OH)<sub>3</sub>.

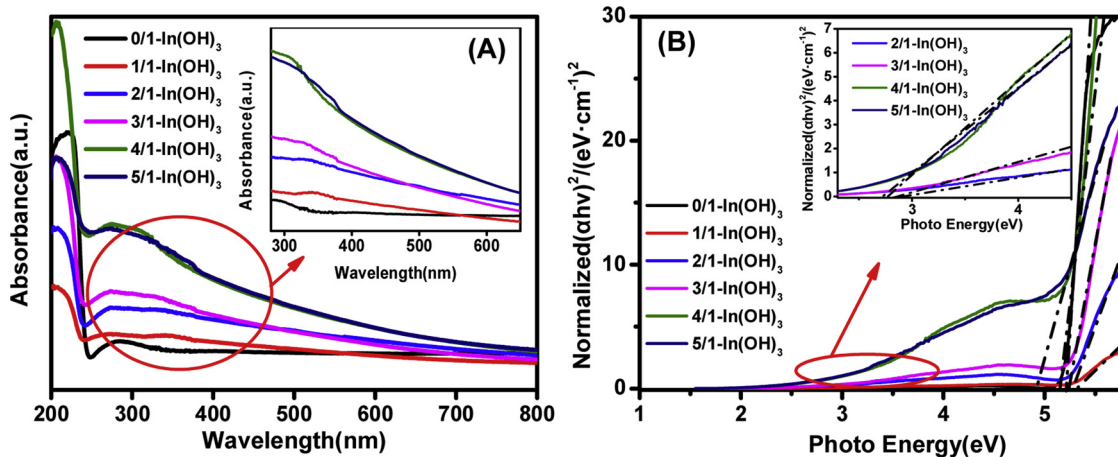


**Fig. 6.** (A) UV-vis diffused reflectance spectra; (B) plot of the transformed Kubelka-Munk function versus the photon energy.

while later one is created by In vacancy. It's also consistent with above results.

In order to further analyze the energy band structure of In(OH)<sub>3</sub>, Mott-Schottky plots (M-S) are employed to evaluate the flat-band potential ( $E_{FB}$ ), carrier concentration and the type of semiconductor. According to the following equation,  $E_{FB}$  at electrode-electrolyte interface was estimated [54–56].

$$1/C^2 = (2/\epsilon_r \epsilon_0 e N_d A^2) [(E - E_{FB}) - kT/e]$$

where C is the specific capacity,  $\epsilon_r$  is the dielectric constant of the samples,  $\epsilon_0$  is the electric permittivity of vacuum ( $8.85 \times 10^{-12} \text{ N}^{-1} \text{ C}^2 \text{ m}^{-2}$ ),  $N_d$  is the carrier density of the samples, A is the efficient area of the electrode, E is the applied potential,  $E_{FB}$  is the flat band potential, k is the Boltzmann constant, T is the absolute temperature, and e is electron charge ( $1.602 \times 10^{-19} \text{ C}$ ). The M-S curves of the samples at a frequency of 1 kHz were tested, as shown in Fig. 7-A. All samples exhibited a positive slope, indicating that they are all n-type semiconductors. The flat band potentials of 0/1-In(OH)<sub>3</sub>, 1/1-In(OH)<sub>3</sub>, 2/1-In(OH)<sub>3</sub>, 3/1-In(OH)<sub>3</sub>, 4/1-In(OH)<sub>3</sub>, and 5/1-In(OH)<sub>3</sub> were -0.63, -1.08, -1.13, -1.15, -1.17, and -1.09 V versus Ag/AgCl, respectively. It is apparent that the  $E_{FB}$  of the samples prepared by mixed solution of water and En exhibits a significant negative shift compared to the one prepared in water only solvent. Moreover, slope of M-S curves of former samples significantly reduced compared to the later one, indicating an increase in carrier density. For comparison, the electrode potential was converted to NHE scale using the equation [57,58]:

$$E(\text{NHE}) = E(\text{Ag/AgCl}) + 0.197V$$

It is known that for n-type semiconductor conduction band potential ( $E_{CB}$ ) is more negative than flat band potential with about -0.1 or -0.2 V [23]. According to the bandgap data in Fig. 6-B, the valence band potential ( $E_{VB}$ ) can be estimated by the formula:  $E_{VB} = E_{CB} + E_g$  and listed in Table 2. In addition,  $E_{VB\text{-defect}}$ , attributing to the presence of In vacancies in In(OH)<sub>3</sub>, was also calculated. It acts as an acceptor level for charge carrier and accordingly enhances the visible-light response as well as improves charge carrier separation. This indium defect level is in the middle of bulk In(OH)<sub>3</sub> band gap, which is in well agreement with the double light absorption mechanism. It has been reported that the two-step absorption through the defect state contributes to the edge absorption of the wide gap semiconductor [23]. Therefore, the defect-assisted two-step absorption may be beneficial for the enhancement of visible-light photocatalytic activity of In(OH)<sub>3</sub> in this work.

In order to further investigate the photoelectric properties of In(OH)<sub>3</sub>, a series of photoelectrochemical tests were carried out. The transient photocurrent response with several on-off cycles was recorded under Xe lamp illumination as shown in Fig. 7-B. In(OH)<sub>3</sub>

prepared with water only solvent exhibits a small photocurrent intensity. After the addition of En, the photocurrent intensity of In(OH)<sub>3</sub> enhanced and reached the maximum value when the ratio of En/water is 4:1. It can be attributed to the improvement of both light absorption and separation efficiency of photogenerated carriers due to the existence of defect sites. However, further increasing the En content in solvent (5/1-In(OH)<sub>3</sub>) led to declined photocurrent intensity, indicating that excessive amount of vacancies promoted the recombination rate of photogenerated carriers.

The electron transfer properties were continued to be evaluated using classical cyclic voltammetry as shown in Fig. 7-C. The CV curve area is determined by the amount of charge transferred into and out of the electrode during the scan [59,60]. In general, the greater the amount of charge passed through, the stronger the ability of charge transfer was. It was found that after the addition of En, the CV curve area slightly increased and 4/1-In(OH)<sub>3</sub> shows the largest CV curve area, revealing that the electron transfer rate is the fastest, which was well consistent with the result of photocurrent response. In addition, electrochemical impedance spectroscopy (EIS) of In(OH)<sub>3</sub> photoelectrodes were also obtained as shown in Fig. 7-D. The sample 4/1-In(OH)<sub>3</sub> shows a significant reduction in the arc radius of the Nyquist curve, meaning that it has low interfacial resistance and high charge-carrier separation efficiency [56]. These results are attributed to the enhancement in absorption of visible light, increase in specific surface area, and decrease in the recombination rate of photogenerated electron-hole pairs.

### 3.3. Chemisorption of CO<sub>2</sub> on In(OH)<sub>3</sub>

The photocatalytic activity of CO<sub>2</sub> reduction with H<sub>2</sub>O strongly depends on the interaction between CO<sub>2</sub> molecules and photocatalysts and adsorbed amount of reactive species such as m-CO<sub>3</sub><sup>2-</sup> or b-CO<sub>3</sub><sup>2-</sup>. Herein, to investigate the species and amount of CO<sub>2</sub> intermediates, in situ FT-IR spectra after CO<sub>2</sub> adsorption in the dark environment for 2 h were performed. As shown in Fig. 8, there was almost no adsorption band for 0/1-In(OH)<sub>3</sub> sample. Two samples prepared in mixed solutions have seven obvious FT-IR bands at around 1678, 1644, 1585, 1513, 1442, 1387, and 1345 cm<sup>-1</sup>. The band at 1678 cm<sup>-1</sup> is related to the O-H vibrating of adsorbed H<sub>2</sub>O. The weak bands at 1644 and 1442 cm<sup>-1</sup> are assigned to bidentate bicarbonate (b-HCO<sub>3</sub><sup>2-</sup>) [61–64], which can be derived from the reaction between adsorbed CO<sub>2</sub> and H<sub>2</sub>O or OH. The bands at 1585 and 1345 cm<sup>-1</sup> are attributed to bidentate carbonate (b-CO<sub>3</sub><sup>2-</sup>) [65,66]. The bands at 1513 and 1387 cm<sup>-1</sup> correspond to the asymmetric and symmetric O=C=O stretches of m-CO<sub>3</sub><sup>2-</sup> [67]. Surface CO<sub>2</sub> species mainly resulted from the bonding of CO<sub>2</sub> molecule to the surface oxygen atom in In vacancies of photocatalyst by carbon atom, which can be transformed to surface m-CO<sub>3</sub><sup>2-</sup>.

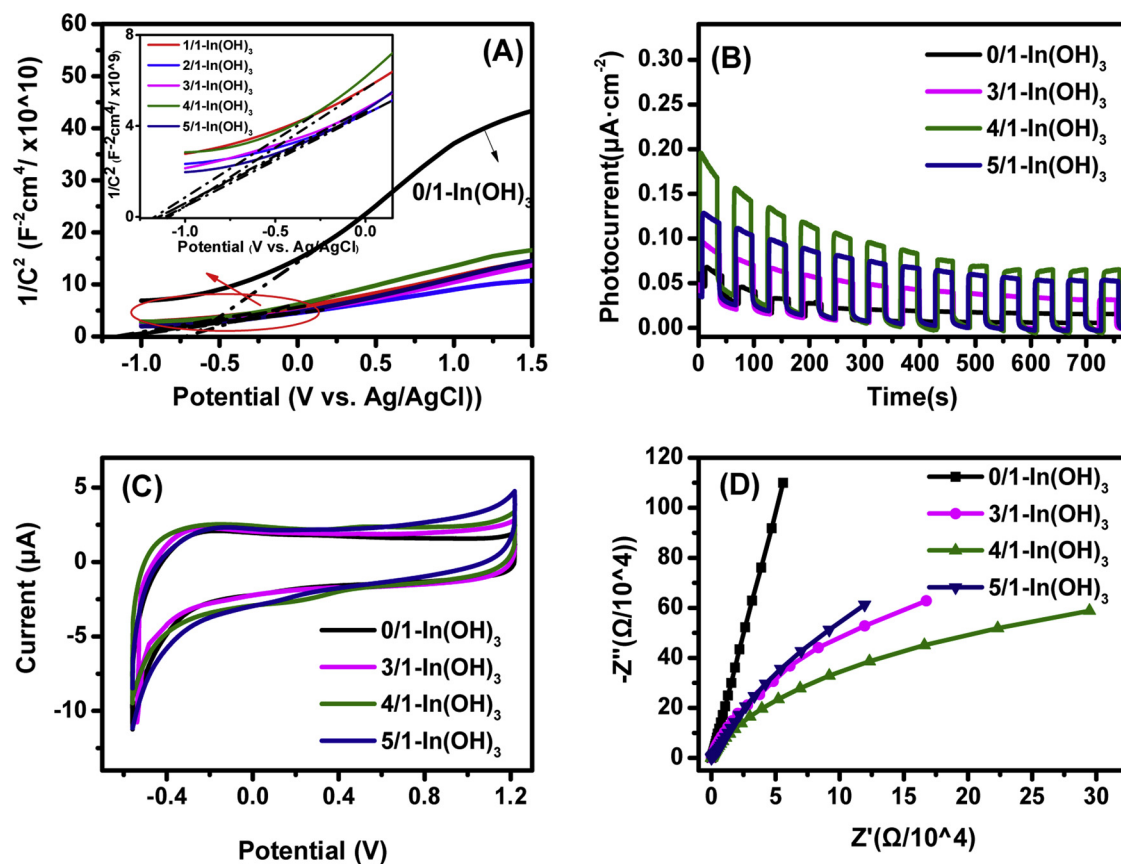


**Fig. 7.** (A) Mott-Schottky plots of In(OH)<sub>3</sub> series at frequency 1.0 kHz ; (B) Photocurrent response; (C) CV curves; (D) Electrochemical impedance measurements of In(OH)<sub>3</sub> series.

**Table 2**  
The band gap, the position of conduction band and valence band.

Catalysts	Band gap / (eV)	Defect energy / (eV)	$E_{FB}$ / (V vs. NHE)	$E_{CB}$ / (V vs. NHE)	$E_{VB}$ / (V vs. NHE)	$E_{VB-}$ / (V vs. NHE)
0/1-In(OH) <sub>3</sub>	5.21	—	-0.43	-0.63	4.58	—
1/1-In(OH) <sub>3</sub>	5.32	—	-0.88	-1.08	4.24	—
2/1-In(OH) <sub>3</sub>	5.28	2.89	-0.94	-1.14	4.14	1.29
3/1-In(OH) <sub>3</sub>	5.24	2.84	-0.96	-1.16	4.08	1.28
4/1-In(OH) <sub>3</sub>	5.15	2.76	-0.97	-1.17	3.98	1.22
5/1-In(OH) <sub>3</sub>	4.92	2.71	-0.89	-1.09	3.83	1.12

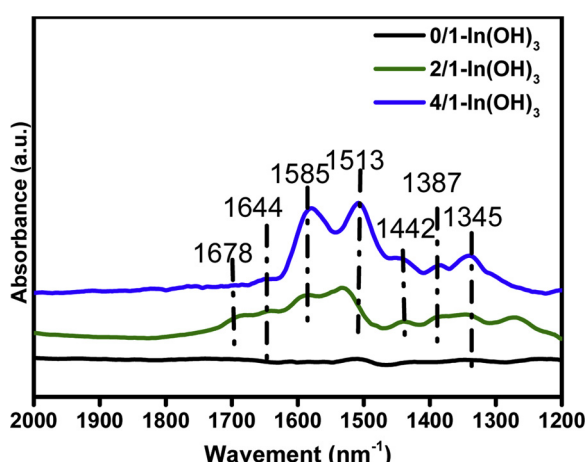


**Fig. 8.** In situ DRIFTS spectra of CO<sub>2</sub> adsorption on In(OH)<sub>3</sub>.

species. m – CO<sub>3</sub><sup>2-</sup> species can be further converted to b – CO<sub>3</sub><sup>2-</sup> species by bonding to metal centers of In(OH)<sub>3</sub> through one oxygen atom in m – CO<sub>3</sub><sup>2-</sup> species. Obviously, 4/1-In(OH)<sub>3</sub> presents much stronger absorption band than 2/1-In(OH)<sub>3</sub>, suggesting its more CO<sub>2</sub> adsorption amount, which is due to the higher vacancy concentration over 4/1-In(OH)<sub>3</sub> than 2/1-In(OH)<sub>3</sub>. In addition, the band for b – CO<sub>3</sub><sup>2-</sup> species at 1585 cm<sup>-1</sup> and that for m – CO<sub>3</sub><sup>2-</sup> species at 1513 cm<sup>-1</sup> over 4/1-In(OH)<sub>3</sub> red-shifted to lower wavenumber compared to 2/1-In(OH)<sub>3</sub>, revealing the weaker O=C=O stretches and the stronger adsorption bonds. This phenomenon is mainly due to the fact that the higher vacancy concentration could increase the basicity of the photocatalyst surface, which improves the adsorption of CO<sub>2</sub> on catalyst surface, and activating O=C bond.

#### 3.4. Photocatalytic activity

The activities of In(OH)<sub>3</sub> series catalysts for photocatalytic reduction of CO<sub>2</sub> were evaluated under visible light irradiation at 200 °C using water as reducing agent. The control experiments were carried out firstly and confirmed that both the light irradiation and photocatalyst were essential for CO<sub>2</sub> photoreduction. Besides, only H<sub>2</sub> and O<sub>2</sub> was detected when the high purity N<sub>2</sub> replaced CO<sub>2</sub> in the reaction system, suggesting that the formed carbon-containing products originated from CO<sub>2</sub> but not contamination.

H<sub>2</sub>, CO, CH<sub>4</sub>, and O<sub>2</sub> were detected to be the major CO<sub>2</sub> reduction products and the evolution rates were illustrated in Fig. 9-A. In(OH)<sub>3</sub> prepared with water only solvent shows relatively lower H<sub>2</sub>, CO and CH<sub>4</sub> production rates (3.7, 3.2 and 5.7 μmol/g<sub>cat</sub>/h, respectively). In contrast, all other In(OH)<sub>3</sub> samples prepared with mixed solution of En and water exhibit much higher H<sub>2</sub>, CO and CH<sub>4</sub> production rates. Production rates of H<sub>2</sub> are 8.7, 13.7, 10.8, 15.3, and 8.3 μmol/g<sub>cat</sub>/h,

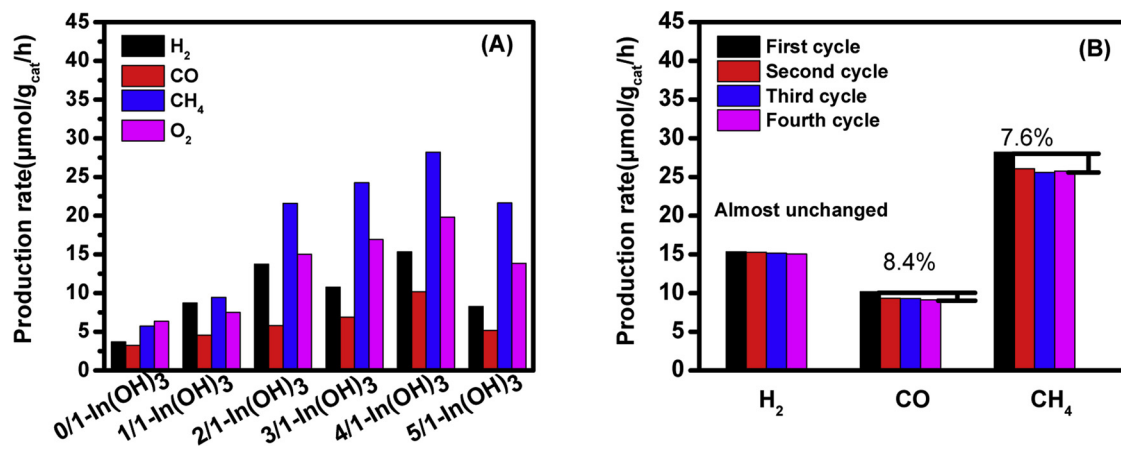


Fig. 9. (A) Production rates of  $\text{CO}$ ,  $\text{H}_2$ ,  $\text{CH}_4$  and  $\text{O}_2$  over  $\text{In(OH)}_3$  samples prepared with different ratios of En/water; (B) Photocatalytic production rates of  $\text{CO}$ ,  $\text{H}_2$ ,  $\text{CH}_4$  in four cycles over 4/1-In(OH)<sub>3</sub>.

those of  $\text{CO}$  are 4.6, 5.8, 6.9, 10.2, and  $5.2 \mu\text{mol/g}_{\text{cat}}/\text{h}$ , those of  $\text{CH}_4$  are 9.5, 21.6, 24.3, 28.2, and  $21.7 \mu\text{mol/g}_{\text{cat}}/\text{h}$  for 1/1-In(OH)<sub>3</sub>, 2/1-In(OH)<sub>3</sub>, 3/1-In(OH)<sub>3</sub>, 4/1-In(OH)<sub>3</sub>, and 5/1-In(OH)<sub>3</sub>, respectively. In general, the activity of photocatalytic reduction of  $\text{CO}_2$  first increased, and then decreased with the increase of En content in solvent. 4/1-In(OH)<sub>3</sub> sample illustrates the highest photocatalytic activity for  $\text{CO}_2$  reduction. Moreover, we did the stability test over 4/1-In(OH)<sub>3</sub> for four cycles (16 h) and the results are shown in Fig. 9 (B). It's clear that the catalyst kept stable after running four cycles under experimental condition. The production rate of  $\text{H}_2$ ,  $\text{CO}$ , and  $\text{CH}_4$  was observed to be ~100%, > 90%, and > 90%, respectively, of that from fresh sample.

The enhancement of photocatalytic performance of  $\text{In(OH)}_3$  prepared in En containing solvent can be ascribed to two facts. Firstly, the introduction of En changed morphology, reduced particle sizes and increased amount of mesopores of  $\text{In(OH)}_3$ , which increased specific surface area and amount of active sites. All above are beneficial for the improvement of a catalyst's performance. Secondly, the presence of En in hydrothermal solvent boosted the formation of In vacancies on the  $\text{In(OH)}_3$  surface, which improved light absorption, increased  $\text{CO}_2$  chemisorption, and inhibited recombination of photogenerated electrons and holes. These promoted photo-related properties enhanced the photocatalytic efficiency. Moreover, it is worth noting that a suitable amount of En addition is critical for optimizing reaction performance of  $\text{In(OH)}_3$  for photocatalytic reduction of  $\text{CO}_2$ . Firstly, excessive En (the case in 5/1-In(OH)<sub>3</sub>) would decrease the pore amount and surface area, which finally hinder its reaction performance. On the other hand, excessive En would produce lots of amounts of defects, which act as recombination centers for charge carriers leading to the decline of photocatalytic activity. Therefore, adjusting the ratio of En and water in mixed solvent is an effective approach to regulate the defect concentration on  $\text{In(OH)}_3$  surface and accordingly optimize the reaction performance.

We also investigated the composition of the sample after the reaction. XRD patterns suggest that there is no any other phase or impurity in the post-reaction sample, indicating that the post-reaction sample is still with pure body-centered cubic structure. Compared to the fresh sample, the first weight loss step locating at < 200 °C (TG curve in Fig. 10-B), resulting from the desorption of En and water, disappeared. It can be attributed to the pretreatment before light irradiation at relatively high temperature (200 °C). The second weight loss between 280–300°C is about 16.63%, which is consistent with the theoretical weight loss value (16%) of conversion of  $\text{In(OH)}_3$  to  $\text{In}_2\text{O}_3$ . It further confirms that the structure of post-reaction sample is still  $\text{In(OH)}_3$ . According to the above characterizations,  $\text{In(OH)}_3$  does not undergo a phase change, and the catalytic activity of the photocatalytic reduction of  $\text{CO}_2$  is derived from  $\text{In(OH)}_3$  instead of other phases.

On the basis of above results, a possible underlying photocatalytic mechanism is proposed in Scheme 2 (use 4/1-In(OH)<sub>3</sub> as example). Under visible light irradiation, the 4/1-In(OH)<sub>3</sub> achieves the visible-light photocatalytic activity through the two-step absorption mechanism. It results from the presence of In vacancy defects, which narrows the energy band gap. Firstly, the initial electrons are excited to indium vacancy defect energy level from VB of  $\text{In(OH)}_3$ . Then, the excited electrons further photoexcited to the CB of  $\text{In(OH)}_3$  by absorbing photons for  $\text{CO}_2$  reduction with  $\text{H}_2\text{O}$ . At the same time, the holes left on the VB are consumed by the electron donor ( $\text{H}_2\text{O}$ ), leading to a highly efficient photocatalytic reduction activity for  $\text{CO}_2$ .

#### 4. Conclusion

In this work, a series of  $\text{In(OH)}_3$  with abundant indium vacancies were synthesized by hydrothermal method using mixed solution of ethylenediamine(En) and water for photocatalytic reduction of  $\text{CO}_2$  with  $\text{H}_2\text{O}$  vapor. The morphology, particle size, crystallinity, pore structure, and vacancy concentration were successfully regulated by adjusting the ratio of En and water in mixed solvent, which were characterized by XRD, FT-IR, TG-DTA, SEM, HRTEM, UV-vis DRS, PL spectra, XPS and EPR. Moreover, the effect of En/water ration on the adsorption capacity of  $\text{CO}_2$  and photo-electrical properties of  $\text{In(OH)}_3$  were further investigated by in-situ FTIR, PL spectra, UV-vis DRS, CV, and EIS. The visible-light response is attributed to two-photo excitation by the two-step absorption mechanism resulting from the In defect sites which narrow energy band gap.  $\text{In(OH)}_3$  prepared in mixed solution exhibited much higher photocatalytic activities compared to that prepared in water only solvent. The enhancement is ascribed to two facts. Firstly, the introduction of En changed increases specific surface area as well as the amount of active sites. Secondly, the presence of En boosts the formation of a large number In vacancies on the surface of  $\text{In(OH)}_3$ , which improves light absorption, increases chemisorption of  $\text{CO}_2$ , and suppresses recombination of photogenerated electrons and holes. With optimal En/water ratio (4:1), In-vacancy engineered plate-like  $\text{In(OH)}_3$  exhibits the highest photocatalytic activity for  $\text{CO}_2$  reduction with  $\text{H}_2$ ,  $\text{CO}$ , and  $\text{CH}_4$  formation rates of 15.33, 10.18, and  $28.20 \mu\text{mol/g}_{\text{cat}}/\text{h}$ , respectively under visible light irradiation.

#### Acknowledgements

We gratefully acknowledge the financial supports from the National Natural Science Foundation of China (No. 21276190 and 20806059) and Tianjin Natural Science Foundation (15 JCYBJC20900).

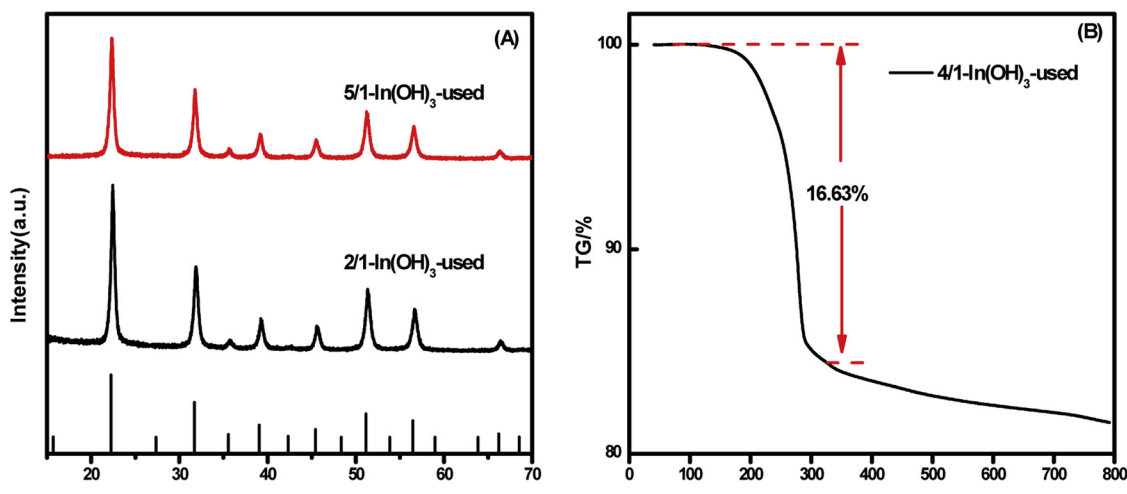
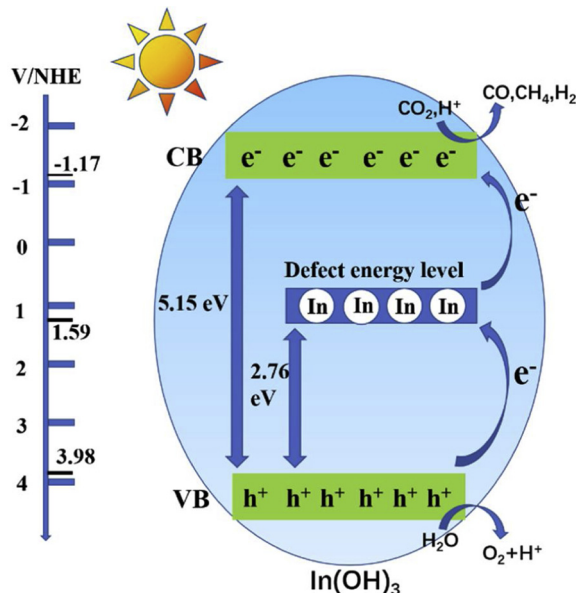


Fig. 10. (A) XRD patterns; (B) Thermal weight loss curves.

Scheme 2. The mechanism of photocatalytic reduction of CO<sub>2</sub> with H<sub>2</sub>O vapor over 4/1-In(OH)<sub>3</sub>.

## References

- [1] W. Shi, X. Guo, C. Cui, K. Jiang, Z. Li, L. Qu, J. Wang, Controllable synthesis of Cu<sub>2</sub>O decorated WO<sub>3</sub> nanosheets with dominant (001) facets for photocatalytic CO<sub>2</sub> reduction under visible -light irradiation, *Appl. Catal. B-Environ.* 243 (2019) 236–242.
- [2] N. Shehzad, M. Tahir, K. Johari, T. Murugesan, M. Hussain, A critical review on TiO<sub>2</sub> based photocatalytic CO<sub>2</sub> reduction system: strategies to improve efficiency, *J. CO<sub>2</sub> Util.* 26 (2018) 98–122.
- [3] H. Wei, W.A. McMaster, J.Z.Y. Tan, L. Cao, D. Chen, R.A. Caruso, Mesoporous TiO<sub>2</sub>/g-C<sub>3</sub>N<sub>4</sub> microspheres with enhanced visible-light photocatalytic activity, *J. Phys. Chem. C* 121 (2017) 22114–22122.
- [4] W. Dai, X. Hu, T. Wang, W. Xiong, X. Luo, J. Zou, Hierarchical CeO<sub>2</sub>/Bi<sub>2</sub>MoO<sub>6</sub> heterostructured nanocomposites for photoreduction of CO<sub>2</sub> into hydrocarbons under visible light irradiation, *Appl. Surf. Sci.* 434 (2018) 481–491.
- [5] Y. Li, C. Wang, M. Song, D. Li, X. Zhang, Y. Li, U. TiO<sub>2(2,x)</sub>/Co<sub>0</sub>x photocatalyst sparkles in photothermocatalytic reduction of CO<sub>2</sub> with H<sub>2</sub>O steam, *Appl. Catal. B-Environ.* 243 (2019) 760–770.
- [6] S. Nahar, M.F.M. Zain, A.A.H. Kadhum, H.A. Hasan, M.R. Hasan, Advances in photocatalytic CO<sub>2</sub> reduction with water: a review, *Materials* 10 (2017).
- [7] M. Edelmannova, K. Lin, J.C.S. Wu, I. Troppova, L. Capek, K. Koci, Photocatalytic hydrogenation and reduction of CO<sub>2</sub> over CuO/TiO<sub>2</sub> photocatalysts, *Appl. Surf. Sci.* 454 (2018) 313–318.
- [8] L. Lin, C. Hou, X. Zhang, Y. Wang, Y. Chen, T. He, Highly efficient visible-light driven photocatalytic reduction of CO<sub>2</sub> over g-C<sub>3</sub>N<sub>4</sub> nanosheets/tetra(4-carboxyphenyl)porphyrin iron(III) chloride heterogeneous catalysts, *Appl. Catal. B-Environ.* 221 (2018) 312–319.
- [9] H. Wang, L. Zhang, K. Wang, X. Sun, W. Wang, Enhanced photocatalytic CO<sub>2</sub> reduction to methane over WO<sub>(3)(0.33)</sub>H<sub>2</sub>O via Mo doping, *Appl. Catal. B-Environ.* 243 (2019) 771–779.
- [10] W. Tu, Y. Zhou, Z. Zou, Development of adjusting semiconductor nanostructures for photocatalytic reduction of CO<sub>2</sub>, *Imaging Sci. Photochem.* 33 (2015) 347–357.
- [11] Y. Zhao, W. Liu, Z. Zhang, X. Zhu, Analysis of factors affecting photocatalytic reduction of CO<sub>2</sub>, *Electric Power* 46 (2013) 90–95.
- [12] G. Capilli, M. Costamagna, F. Sordello, C. Minero, Synthesis, characterization and photocatalytic performance of p-type carbon nitride, *Appl. Catal. B-Environ.* 242 (2019) 121–131.
- [13] X.Y. Kong, Y.Y. Choo, S. Chai, A.K. Soh, A.R. Mohamed, Oxygen vacancy induced Bi<sub>2</sub>WO<sub>6</sub> for the realization of photocatalytic CO<sub>2</sub> reduction over the full solar spectrum: from the UV to the NIR region, *Chem. Commun.* 52 (2016) 14242–14245.
- [14] Y. Pan, Z. Sun, H. Cong, Y. Men, S. Xin, J. Song, S. Yu, Photocatalytic CO<sub>2</sub> reduction highly enhanced by oxygen vacancies on Pt-nanoparticle-dispersed gallium oxide, *Nano Res.* 9 (2016) 1689–1700.
- [15] M. Liang, T. Borjigin, Y. Zhang, B. Liu, H. Liu, H. Guo, Controlled assemble of hollow heterostructured g-C<sub>3</sub>N<sub>4</sub>@CeO<sub>2</sub> with rich oxygen vacancies for enhanced photocatalytic CO<sub>2</sub> reduction, *Appl. Catal. B-Environ.* 243 (2019) 566–575.
- [16] C. Xin, M. Hu, K. Wang, X. Wang, Significant enhancement of photocatalytic reduction of CO<sub>2</sub> with H<sub>2</sub>O over ZnO by the formation of basic zinc carbonate, *Langmuir* 33 (2017) 6667–6676.
- [17] Q. Liu, Q. Zhang, B. Liu, S. Li, J. Ma, Building surface defects by doping with transition metal on ultrafine TiO<sub>2</sub> to enhance the photocatalytic H<sub>2</sub> production activity, *Chin. J. Catal.* 39 (2018) 542–548.
- [18] Z. Yi, X. Xu, X. Duan, W. Zhu, Z. Zhou, X. Fan, Photocatalytic activity and stability of ZnO particles with different morphologies, *Rare Met.* 30 (2011) 183–187.
- [19] A. Pu, J. Deng, M. Li, J. Gao, H. Zhang, Y. Hao, J. Zhong, X. Sun, Coupling Ti-doping and oxygen vacancies in hematite nanostructures for solar water oxidation with high efficiency, *J. Mater. Chem. A* 2 (2014) 2491–2497.
- [20] X. Zhang, L. Zhao, C. Fan, Z. Liang, P. Han, Effects of oxygen vacancy on the electronic structure and absorption spectra of bismuth oxychloride, *Comp. Mater. Sci.* 61 (2012) 180–184.
- [21] D. Jiang, L. Zhu, R.M. Irfan, L. Zhang, P. Du, Integrating noble-metal-free NiS co-catalyst with a semiconductor heterojunction composite for efficient photocatalytic H<sub>2</sub> production in water under visible light, *Chin. J. Catal.* 38 (2017) 2102–2109.
- [22] Y. Zhu, J. Li, T. Ma, Y. Liu, G. Du, Z. Yuan, Sonochemistry-assisted synthesis and optical properties of mesoporous ZnS nanomaterials, *J. Mater. Chem. A* 2 (2014) 1093–1101.
- [23] X. Hao, J. Zhou, Z. Cui, Y. Wang, Y. Wang, Z. Zou, Zn-vacancy mediated electron-hole separation in ZnS/g-C<sub>3</sub>N<sub>4</sub> heterojunction for efficient visible-light photocatalytic hydrogen production, *Appl. Catal. B-Environ.* 229 (2018) 41–51.
- [24] J. Liu, S. Xie, Z. Geng, K. Huang, L. Fan, W. Zhou, L. Qiu, D. Gao, L. Ji, L. Duan, L. Lu, W. Li, S. Bai, Z. Liu, W. Chen, S. Feng, Y. Zhang, Carbon nitride supramolecular hybrid material enabled high-efficiency photocatalytic water treatments, *Nano Lett.* 16 (2016) 6568–6575.
- [25] F. Dong, X. Xiao, G. Jiang, Y. Zhang, W. Cui, J. Ma, Surface oxygen-vacancy induced photocatalytic activity of La(OH)<sub>3</sub> nanorods prepared by a fast and scalable method, *Phys. Chem. Chem. Phys.* 17 (2015) 16058–16066.
- [26] T. Sato, Preparation and thermal decomposition of indium hydroxide, *J. Therm. Anal. Calorim.* 82 (2005) 775–782.
- [27] K.K. Ghuman, T.E. Wood, L.B. Hoch, C.A. Mims, G.A. Ozin, C.V. Singh, Illuminating CO<sub>2</sub> reduction on frustrated Lewis pair surfaces: investigating the role of surface hydroxides and oxygen vacancies on nanocrystalline In<sub>2</sub>O<sub>3-x</sub>(OH)<sub>y</sub>, *Phys. Chem. Chem. Phys.* 17 (2015) 14623–14635.
- [28] L.B. Hoch, L. He, Q. Qiao, K. Liao, L.M. Reyes, Y. Zhu, G.A. Ozin, Effect of precursor selection on the photocatalytic performance of indium oxide nanomaterials for gas-phase CO<sub>2</sub> reduction, *Chem. Mater.* 28 (2016) 4160–4168.
- [29] M. Tahir, N.S. Amin, Photocatalytic CO<sub>2</sub> reduction with H<sub>2</sub> as reductant over copper and indium co-doped TiO<sub>2</sub> nanocatalysts in a monolith photoreactor, *Appl. Catal. A*

Gen. 493 (2015) 90–102.

[30] M.A. Gondal, M.A. Dastageer, L.E. Oloore, U. Baig, Laser induced selective photocatalytic reduction of CO<sub>2</sub> into methanol using In<sub>2</sub>O<sub>3</sub>-WO<sub>3</sub> nano-composite, *J. Photochem. Photobiol. A* 343 (2017) 40–50.

[31] M. Tahir, N.S. Amin, Photocatalytic CO<sub>2</sub> reduction with H<sub>2</sub> as reductant over copper and indium co-doped TiO<sub>2</sub> nanocatalysts in a monolith photoreactor, *Appl. Catal. A-Gen.* 493 (2015) 90–102.

[32] D. Chakraborty, S. Kaleemulla, N.M. Rao, G.V. Rao, Synthesis and magnetic properties of (Fe, Sn) co-doped In<sub>2</sub>O<sub>3</sub> nanoparticles, *J. Mater. Sci. Mater. El* 28 (2017) 18977–18985.

[33] Y. Wang, J. Zhao, Y. Li, C. Wang, Selective photocatalytic CO<sub>2</sub> reduction to CH<sub>4</sub> over Pt/In<sub>2</sub>O<sub>3</sub>: significant role of hydrogen adatom, *Appl. Catal. B-Environ.* 226 (2018) 544–553.

[34] X. Gan, R. Zheng, T. Liu, J. Meng, R. Chen, X. Sun, X. Sun, N-doped mesoporous In<sub>2</sub>O<sub>3</sub> for photocatalytic oxygen evolution from the in-based metal-organic frameworks, *Chem. Eur. J.* 23 (2017) 7264–7271.

[35] N. Rui, Z. Wang, K. Sun, J. Ye, Q. Ge, C. Liu, CO<sub>2</sub> hydrogenation to methanol over Pd/In<sub>2</sub>O<sub>3</sub>: effects of Pd and oxygen vacancy, *Appl. Catal. B-Environ.* 218 (2017) 488–497.

[36] H.L. Zhu, K.H. Yao, Y.H. Wo, N.Y. Wang, L. Wang, Hydrothermal synthesis of single crystalline In(OH)<sub>3</sub> nanorods and their characterization, *Semicond. Sci. Technol.* 19 (2004) 1020–1023.

[37] Q. Huang, W. Huang, C. Xu, B. Wang, X. Wang, J. Tu, Y. Cao, Synthesis of hierarchical In(OH)<sub>3</sub> and application in electrochemical sensing properties of uric acid, *J. Funct. Mater.* 47 (2016) 10113–10117.

[38] H. Zhu, X. Wang, L. Qian, F. Yang, X. Yang, Nanoporous In<sub>2</sub>O<sub>3</sub> nanocrystal clusters: one-step synthesis, thermal stability and optical property, *J. Phys. Chem. C* 112 (2008) 4486–4491.

[39] Y. Wang, W. Liu, Infrared Absorption Spectra and Thermal Stabilities Of Transition-Metal-Ethylenediamine Complexes vol. 8, (1993), pp. 30–34.

[40] C. Li, G. Liu, S. Liu, One-step hydrothermal synthesis of high active mesoporous nanocubes of In(OH)<sub>3</sub> with high photocatalytic activity, *J. Funct. Mater.* 45 (2014) 6144–6147 6152.

[41] J. Guo, S. Ouyang, T. Kako, J. Ye, Mesoporous In(OH)<sub>3</sub> for photoreduction of CO<sub>2</sub> into renewable hydrocarbon fuels, *Appl. Surf. Sci.* 280 (2013) 418–423.

[42] H. Yang, Z. Yang, H. Liang, L. Liu, J. Guo, Y. Yang, Solvothermal synthesis of In(OH)<sub>3</sub> nanorods and their conversion to In<sub>2</sub>O<sub>3</sub>, *Mater. Lett.* 64 (2010) 1418–1420.

[43] Q. Li, J. Yang, D. Feng, Z. Wu, Q. Wu, S.S. Park, C. Ha, D. Zhao, Facile synthesis of porous carbon nitride spheres with hierarchical three-dimensional mesostructures for CO<sub>2</sub> capture, *Nano Res.* 3 (2010) 632–642.

[44] N.R. Khalid, E. Ahmed, N.A. Niaz, G. Nabi, M. Ahmad, M.B. Tahir, M. Rafique, M. Rizwan, Y. Khan, Highly visible light responsive metal loaded N/TiO<sub>2</sub> nanoparticles for photocatalytic conversion of CO<sub>2</sub> into methane, *Ceram. Int.* 43 (2017) 6771–6777.

[45] Z. Shi, W. Wang, Z. Zhang, Synthesis and characterization of indium hydroxide truncated polyhedral microcrystals, *Mater. Lett.* 62 (2008) 4293–4295.

[46] L. Hao, J. Yan, S. Guan, L. Cheng, Q. Zhao, Z. Zhu, Y. Wang, Y. Lu, J. Liu, Oxygen vacancies in TiO<sub>2</sub>/SnO<sub>x</sub> coatings prepared by ball milling followed by calcination and their influence on the photocatalytic activity, *Appl. Surf. Sci.* 466 (2019) 490–497.

[47] P. Gao, X. Tian, Y. Nie, C. Yang, Z. Zhou, Y. Wang, Promoted peroxymonosulfate activation into singlet oxygen over perovskite for ofloxacin degradation by controlling the oxygen defect concentration, *Chem. Eng. J.* 359 (2019) 828–839.

[48] S.M. Wu, X.L. Liu, X.L. Lian, G. Tian, C. Janiak, Y.X. Zhang, Y. Lu, H.Z. Yu, J. Hu, H. Wei, H. Zhao, G.G. Chang, G. Van Tendeloo, L.Y. Wang, X.Y. Yang, B.L. Su, Homojunction of oxygen and titanium vacancies and its interfacial n-p effect, *Adv. Mater.* 30 (2018) e1802173.

[49] T. Yan, J. Long, Y. Chen, X. Wang, D. Li, X. Fu, Indium hydroxide: a highly active and low deactivated catalyst for photoinduced oxidation of benzene, *CR Chim.* 11 (2008) 101–106.

[50] L.B. Hoch, P. Szymanski, K.K. Ghuman, L. He, K. Liao, Q. Qiao, L.M. Reyes, Y. Zhu, M.A. El-Sayed, C.V. Singh, G.A. Ozin, Carrier dynamics and the role of surface defects: designing a photocatalyst for gas-phase CO<sub>2</sub> reduction, *Proc. Natl. Acad. Sci. U. S. A.* 113 (2016) E8011–E8020.

[51] Q. Wang, K. Wang, L. Zhang, H. Wang, W. Wang, Photocatalytic reduction of CO<sub>2</sub> to methane over PtO<sub>x</sub>-loaded ultrathin Bi<sub>2</sub>WO<sub>6</sub> nanosheets, *Appl. Surf. Sci.* 470 (2019) 832–839.

[52] R. Zhang, X. Li, S. Liu, L. Yu, Y. Wu, XPS study of oxygen state in LaMn<sub>y</sub>Co<sub>1-y</sub>O<sub>3</sub> catalyst, *Acta Phys. Sin.* (1994) 720–723.

[53] F.V. Da Motta, A.P. de Azevedo Marques, V.D. de Araujo, M.T. de Souza Tavares, M.R. Bomio Delmonte, C.A. Paskocimas, M.S. Li, R.M. Do Nascimento, E. Longo, Optical characterization of europium-doped indium hydroxide nanocubes obtained by microwave-assisted hydrothermal method, *Mater. Res.-Ibero-Am.* 17 (2014) 933–939.

[54] Y. Feng, J. Shen, Q. Cai, H. Yang, Q. Shen, The preparation and properties of a g-C<sub>3</sub>N<sub>4</sub>/AgBr nanocomposite photocatalyst based on protonation pretreatment, *New J. Chem.* 39 (2015) 1132–1138.

[55] Y. Meng, L. Zhang, H. Jiu, Q. Zhang, H. Zhang, W. Ren, Y. Sun, D. Li, Construction of g-C<sub>3</sub>N<sub>4</sub>/ZIF-67 photocatalyst with enhanced photocatalytic CO<sub>2</sub> reduction activity, *Mater. Sci. Semicond. Proc.* 95 (2019) 35–41.

[56] C.A. Mesa, A. Kafizas, Preparation of a pn heterojunction BiFeO<sub>3</sub>@TiO<sub>2</sub> photocatalyst with a core-shell structure for visible-light photocatalytic degradation, *Chin. J. Catal.* 6 (2017) 1052–1062.

[57] K. Jin, A. Chu, J. Park, D. Jeong, S.E. Jerng, U. Sim, H. Jeong, C.W. Lee, Y. Park, K.D. Yang, G.K. Pradhan, D. Kim, N. Sung, S.H. Kim, K.T. Nam, Partially oxidized Sub-10 nm Mn<sub>0</sub> nanocrystals with high activity for water oxidation catalysis, *Sci. Rep. U. K.* 5 (2015).

[58] G. Zhuang, J. Bai, X. Tao, J. Luo, X. Zhou, W. Chen, X. Zhong, X. Li, J. Wang, Trace phosphorus-doping significantly improving S-content of binary-doped mesoporous carbon network with enhancing electrochemical performance, *Microporous Mesoporous Mater.* 256 (2018) 75–83.

[59] A. Abdelwahab, J. Castelo-Quiben, M. Perez-Cadenas, A. Elmouawahidi, F.J. Maldonado-Hodar, F. Carrasco-Marín, A.F. Perez-Cadenas, Cobalt-doped carbon gels as electro-catalysts for the reduction of CO<sub>2</sub> to hydrocarbons, *Catalysts* 7 (2017).

[60] C. Han, J. Li, Z. Ma, H. Xie, G.I.N. Waterhouse, L. Ye, T. Zhang, Black phosphorus quantum dot/g-C<sub>3</sub>N<sub>4</sub> composites for enhanced CO<sub>2</sub> photoreduction to CO, *Sci. China Mater.* 61 (2018) 1159–1166.

[61] W. Chen, C. Wang, W. Ying, In-situ DR-FTIR of CO and CO<sub>2</sub> chemisorptive properties over Rh-Mn-Li/SiO<sub>2</sub> catalyst, *J. East China Univ. Sci. Technol.* 5 (2007) 624–628.

[62] L. Liu, C. Zhao, D. Pitts, H. Zhao, Y. Li, CO<sub>2</sub> photoreduction with H<sub>2</sub>O vapor by porous MgO-TiO<sub>2</sub> microspheres: effects of surface MgO dispersion and CO<sub>2</sub> adsorption-desorption dynamics, *Catal. Sci. Technol.* 4 (2014) 1539–1546.

[63] J. Rasko, F. Solymosi, Infrared spectroscopic study of the photoinduced activation of CO<sub>2</sub> on TiO<sub>2</sub> and Rh/TiO<sub>2</sub> catalyst, *J. Phys. Chem.* 98 (1994) 7147–7152.

[64] Y. Kohno, H. Ishikawa, T. Tanaka, T. Funabiki, S. Yoshida, Photoreduction of carbon dioxide by hydrogen over magnesium oxide, *Phys. Chem. Chem. Phys.* 3 (2001) 1108–1113.

[65] D. Cornu, H. Guesmi, J. Krafft, H. Lauron-Pernot, Lewis acid-base interactions between CO<sub>2</sub> and MgO Surface: DFT and DRIFT approaches, *J. Phys. Chem. C* 116 (2012) 6645–6654.

[66] K. Bhattacharyya, A. Danon, B.K. Vijayan, K.A. Gray, P.C. Stair, E. Weitz, Role of the surface lewis acid and base sites in the adsorption of CO<sub>2</sub> on Titania Nanotubes and platinated titania nanotubes: an in situ FT-IR study, *J. Phys. Chem. C* 117 (2013) 12661–12678.

[67] K. Pokrovski, K.T. Jung, A.T. Bell, Investigation of CO and CO<sub>2</sub> adsorption on tetragonal and monoclinic zirconia, *Langmuir* 17 (2001) 4297–4303.